A practical guide to methodological considerations in the controllability of structural brain networks

Teresa M. Karrer[a,b], Jason Z. Kim[b,*], Jennifer Stiso[c,*], Ari E. Kahn[c], Fabio Pasqualetti[d], Ute Habel[a,e,f], and Danielle S. Bassett[b,g,h,i,j,k,l]

[a] *Department of Psychiatry, Psychotherapy and Psychosomatics, Faculty of Medicine, RWTH Aachen, Germany.*
[b] *Department of Bioengineering, School of Engineering & Applied Science, University of Pennsylvania, Philadelphia, PA 19104, USA.*
[c] *Department of Neuroscience, Perelman School of Medicine, University of Pennsylvania, Philadelphia, PA 19104, USA.*
[d] *Department of Mechanical Engineering, University of California, Riverside, CA 92521, USA.*
[e] *JARA - Translational Brain Medicine, Aachen, Germany.*
[f] *Institute of Neuroscience and Medicine: JARA-Institute Brain Structure Function Relationship (INM 10), Research Center Jülich, Jülich, Germany.*
[g] *Department of Physics and Astronomy, College of Arts & Sciences, University of Pennsylvania, Philadelphia, PA 19104, USA.*
[h] *Department of Neurology, Perelman School of Medicine, University of Pennsylvania, Philadelphia, PA 19104, USA.*
[i] *Department of Psychiatry, Perelman School of Medicine, University of Pennsylvania, Philadelphia, PA 19104, USA.*
[j] *Department of Electrical and Systems Engineering, School of Engineering & Applied Science, University of Pennsylvania, Philadelphia, PA 19104, USA.*
[k] *Santa Fe Institute, Santa Fe, NM 87501, USA.*
[l] *To whom correspondence should be addressed: dsb@seas.upenn.edu*
[*] *These two authors contributed equally.*

1 Supplementary Formulas

The following formulas represent the discrete-time versions of the continuous-time formulas presented in the main manuscript. The formulas for average controllability and control energies are valid for both discrete- and continuous-time systems.

Natural dynamics

$$\boldsymbol{x}(t+1) = \boldsymbol{A}\boldsymbol{x}(t) \tag{1}$$

Controlled dynamics

$$\boldsymbol{x}(t+1) = \boldsymbol{A}\boldsymbol{x}(t) + \boldsymbol{B}_\kappa \boldsymbol{u}_\kappa(t) \tag{2}$$

Normalization

$$\boldsymbol{A}_{norm} = \frac{\boldsymbol{A}}{|\lambda(\boldsymbol{A})|_{max} + c} \tag{3}$$

Controllability Gramian

$$\boldsymbol{W}_{\kappa,T} = \sum_{\tau=0}^{T-1} \boldsymbol{A}^\tau \boldsymbol{B}_\kappa \boldsymbol{B}_\kappa^\top (\boldsymbol{A}^\top)^\tau \tag{4}$$

Modal controllability

$$\phi_i = \sum_{j=1}^{N} (1 - \lambda_j^2(\boldsymbol{A})) v_{ij}^2 \tag{5}$$

Minimum control energy input

$$\boldsymbol{u}(t)_\kappa^* = \operatorname*{argmin}_{\boldsymbol{u}(t)_\kappa} \sum_{t=0}^{T-1} \boldsymbol{u}_\kappa(t)^\top \boldsymbol{u}_\kappa(t) \tag{6}$$

2 Supplementary Methods

2.1 Derivation of modal controllability for continuous-time systems

Consider a discrete-time linear time invariant state space system

$$\boldsymbol{x}(t+1) = \boldsymbol{A'}\boldsymbol{x}(t). \tag{7}$$

Modal controllability is defined as

$$\phi_i = \sum_{j=1}^{N}(1 - \lambda_j^2(\boldsymbol{A'}))v_{ij}'^2, \tag{8}$$

where $\lambda_j(\boldsymbol{A'})$ and $\boldsymbol{v}_j'$ are the j-th eigenvalue and eigenvector of $\boldsymbol{A'}$ [1].

Consider a continuous-time linear time invariant state space system

$$\dot{\boldsymbol{x}} = \boldsymbol{A}\boldsymbol{x}. \tag{9}$$

To turn this continuous-time system into a discrete-time system, a ubiquitous method is the *zero-order hold* given by

$$\boldsymbol{x}(t+1) = e^{\boldsymbol{A}\Delta t}\boldsymbol{x}(t). \tag{10}$$

Here, the discrete-time system evolves as a sampled version of the continuous-time system with a sampling interval of Δt. We call λ_j and $\boldsymbol{v}_j$ the eigenvalues and eigenvectors of $\boldsymbol{A}$.

If we compute the discrete-time modal controllability of the zero-order hold system, we obtain

$$\phi_i = \sum_{j=1}^{N}(1 - (e^{\lambda_j(\boldsymbol{A})\Delta t})^2)v_{ij}^2 = \sum_{j=1}^{N}(1 - e^{2\lambda_j(\boldsymbol{A})\Delta t})v_{ij}^2. \tag{11}$$

Here, we require a selection of the sampling rate, Δt. Due to the normalization of our continuous-time systems, the most quickly decaying mode (and thereby most negative eigenvalue) is bounded by $0 > \lambda_N > -1$. Let us consider the worst case scenario where the most quickly decaying mode has exponent -1. Then two-sided Fourier transform of an exponential function e^{-t} is given by

$$\mathcal{F}[e^{-t}] = F(f) = \frac{2}{1 + (2\pi f)^2}, \tag{12}$$

where f is the signal frequency in Hz. The exponential decay has a maximum signal amplitude at $f = 0$, and loses 95% signal amplitude at $f \approx 0.7$Hz. Hence, we use $\Delta t = 0.5$ for a sampling rate of 2Hz to ensure that we capture the majority of the signal amplitudes at Nyquist. This leads to the final form

$$\phi_i = \sum_{j=1}^{N}(1 - e^{\lambda_j(\boldsymbol{A})})v_{ij}^2. \tag{13}$$

2.2 Relation of average controllability and average input energy

Previous work [2] has interpreted $Trace(\boldsymbol{W}_{\kappa,T})$ as proxy for the average input energy to avoid numerical difficulties when controlling only a few nodes in very large systems. Average input energy measures the energy required to drive the system from $\boldsymbol{x}_0$ via a specified set of control nodes to all possible target states $\boldsymbol{x}_T$ with unit norm [3, 4]. Following the discussion in the main text, this metric equals $Trace(\boldsymbol{W}_{\kappa,T}^{-1})$ where the inverse of the controllability Gramian is a map from target states to control energy. Other work describes mathematical bounds on the relationship between $Trace(\boldsymbol{W}_{\kappa,T})$ and $Trace(\boldsymbol{W}_{\kappa,T}^{-1})$ [1]. Please note that the goodness of the bound depends on the distribution of eigenvalues of the controllability Gramian. Particularly when controlling only a subset of brain regions, the eigenvalues of the controllability Gramian span many orders of magnitudes so that $Trace(\boldsymbol{W}_{\kappa,T})$ and $Trace(\boldsymbol{W}_{\kappa,T}^{-1})$ diverge [5].

2.3 Acquisition of diffusion imaging data

High resolution anatomical brain images were collected from 10 healthy young adults (23.9 ± 3.6 years; 20-31 years; 70% female). The participants underwent a 53:24 minute diffusion spectrum imaging (DSI) scan with 730 diffusion directions (maximum b-value = $5010s/mm^2$, 21 b = 0 images, TR = 4300ms, TE = 102ms, matrix size = 144×144, field of view = $260 \times 260mm^2$, slice number = 87, resolution = $1.8×1.8×1.8mm^3$, multi-band acceleration factor = 3). Additionally, T1-weighted images were obtained using an MPRAGE sequence (TR = 2500ms, TE = 2.18ms, flip angle = 7 degrees, slice number = 208, slice thickness = 0.9mm). Both scans were acquired on a Siemens Magnetom Prisma 3 Tesla scanner with a 64-channel head coil. The study was approved by the Institutional Review Board of the University of Pennsylvania and all participants provided informed consent in writing.

2.4 Preprocessing of diffusion imaging data

As previously described in more detail [6], the individual DSI scans were skull-stripped, realigned, and motion-corrected using an improved average b=0 reference image. The preprocessing was implemented in nipype [7] using the Advanced Normalization Tools (ANTs, [8]) for image registration. We quantified the diffusion at different orientations in each voxel using the generalized q-sampling reconstruction method [9] in DSI Studio (dsi-studio.labsolver.org). Based on the derived quantitative anisotropy values, we performed deterministic tractography across the whole-brain [10]. For each participant, we generated 1,000,000 streamlines with a maximum length of 500mm [11] and a maximum turning angle of 35 degrees [12].

2.5 Examining metrics on an individual and regional level

Since network control theory can be utilized to examine controllability differences in both individuals and brain regions, we separately studied the metrics on an individual and regional level. For this purpose, we summarized average controllability, modal controllability, and minimum control energy across either brain regions or individuals to subsequently investigate individual and regional values, respectively (Fig.1F). To estimate the consistency of a metric across parameter choices on an individual (regional) level, we first summarized the metric across brain regions (individuals) and then computed the Pearson correlation between the individual (regional) values obtained with one modeling choice and the individual (regional) values obtained with the second modeling choice; for example, we compare discrete- and continuous-time systems, and we compare two different parameter choices of time horizon T. When evaluating the statistical significance of effects on both levels, please note that individual analyses are based on a limited sample size of 10 participants whereas regional analyses can capitalize on a larger sample size of 233 brain regions.

2.6 Selection of parameter ranges

We examined the impact of four modelling choices on average and modal controllability, and on minimum and optimal control energy. In each examination of the impact of one specific modeling choice, we systematically varied the modeling choice of interest while keeping all other parameters constant. Here, we wish to provide a detailed explanation of how the variable parameter ranges were selected. We followed the general approach that we attempted to include all possible parameter options such as in the examination of time-system or control set size. In cases where this was not possible, we explored the behavior of the metric starting from the modeling choice most commonly used in the literature. Based on the convergence behavior of the metric, we determined the exact parameter ranges. In doing so, we wished to provide comprehensive insights into the impact of the modeling choices on controllability metrics. Please note that the value at which the metrics start to converge does not automatically generalize to other applications of network control theory but instead depends on all aspects of the simulation including the type of neural system modelled and software used. In the following, we explain the selection of the parameter range for each examined modeling choice separately to ensure that other investigators can determine appropriate parameters ranges to investigate in their system.

Regarding the impact of time-system, we capitalized on both available options, i.e. discrete- and continuous-time systems. When examining the influence of time horizon, we started with $T = 1$ which is the smallest possible option in discrete-time systems. The endpoint of the parameter range was selected in an exploratory way so that the metrics appeared to converge. For average controllability, we selected an endpoint at $T = 1000$ on the individual level and at $T = 50$ on the regional level. Additionally, we examined the behavior of infinite time since this commonly used modelling choice allows an observation of the complete impulse response. For control energies, we selected an endpoint at $T = 10$. Regarding the impact of the normalization parameter, we started from the commonly used choice of $c = 1$. We then explored the parameter in an exponential manner in both directions. Finally, we adjusted the parameter range of c in a way that provides approximately equal insight into both control regimes which was the case for $c = 10^{-1}$ to $c = 10^6$. When probing the impact of control set size, we capitalized on the complete range of controlling a single brain region up to all 233 brain regions.

3 Supplementary Results

3.1 Optimal control energy

We observed high correlations between minimum and optimal energy values on both individual and regional levels (SFig. 8). Thus, in the remainder of the main text we simply focused on minimum control energy. For completeness, here we present the findings for optimal control energy. We began by probing the consistency of optimal control energy across time horizons. We observed that optimal control energy first rapidly decreased and then slightly increased with larger time horizons (SFig. 2A). In contrast to the monotonically decreasing minimum control energy, the increasing amount of optimal control energy might be required to additionally constrain the distance of traversed brain states over longer time horizons. Similar to minimum control energy, we found a high consistency between the metrics across a wide range of examined time horizons. Likewise, smaller time horizons demonstrated a different control regime (SFig. 2B) in which optimal control energy was partly anti-correlated with the corresponding metrics at larger time horizons (individual level: $r_{min} = 0.51$, $p = 0.13$; regional level ($r_{min} = -0.61$, $p = 4 \times 10^{-25}$). Subsequently, we investigated the impact of normalization on optimal control energy. On both the individual and regional levels, we observed that with increasing c, minimum control energy and optimal control energy increased (SFig. 3). Similar to minimum control energy, we observed two different control regimes in optimal control energy depending on the normalization (individual level: $r_{min} = 0.86$, $p = 0.0013$; regional level ($r_{min} = 0.61$, $p = 3 \times 10^{-25}$) (SFig. 4).

Next, we compared optimal control energy based on full and partial control node sets. Similar to minimum control energy, optimal control energy and the associated numerical error decreased exponentially with increasing control set size (SFig. 5B). In optimal control energy, the control of at least 29.6 - 30.9% of brain regions yielded reasonably small numerical errors ($N_{VIS} = 69$, $N_{SOM} = 71$, $N_{DOR} = 69$, $N_{VEN} = 72$, $N_{LIM} = 71$, $N_{FPC} = 72$), which was a slightly higher number of control nodes compared to minimum control energy. Control (SFig. 6A) and state trajectories (SFig. 6B) substantially differed between minimum and optimal control in both the partial- and full-brain control scenario. However, similar to minimum control energy, the amount of optimal control energy increased towards the end of the control horizon. In line with minimum control energy, we observed that the distance between current state and target state continuously decreased in full brain control, whereas in partial control the system traversed more distant states before it reached the target state. We again observed a monotonic increase of optimal control energy with increasing distance between initial state and target state (SFig. 6C). The activation of densely connected cognitive systems again required less energy on average than the activation of random states. In the partial control set, we also observed that a subset of the random state transitions involving the activation of weakly connected brain regions required massive amounts of control energy.

Finally, we examined the effect of different structural connectivity measures and their binarized versions on optimal control energy. All of the effects were highly consistent with those reported for minimum control energy (Fig. 5). We first observed that structural networks based on diffusion imaging ($\boldsymbol{A}$) and spatial adjacency ($\boldsymbol{S}$) provided complementary information on individual and regional optimal control energy values as indicated by their Pearson correlation (individual level: $r = 0.36$, $p = 0.30$; regional level: $r = 0.50$, $p = 8 \times 10^{-16}$). Repeated measures ANOVAs revealed significant main effects of matrix type and binarization at a Bonferroni-corrected level of $\alpha = 0.01$; the main effects remained significant when we held the edge-weight distribution constant. Examining the effects in more detail, we observed

that the binarization increased the individual optimal control energy but did not affect the variability of regional optimal control energy (SFig. 7).

3.2 Relation of metrics

How easily a brain network can be steered to different states and the amount of energy required to achieve a specific state transition could prove to be informative markers for pathology in or injury to the central nervous system. The selection of the metric put to the test primarily depends on the specific research question. To elucidate the empirical associations between controllability metrics and control energies in brain networks, we measured the Pearson correlation between each pair of metrics, summarized separately across brain regions (SFig. 8A) and individuals (SFig. 8B and SFig. 8C). In line with previous research [2], average and modal controllability showed a positive, yet non-significant association on the individual level ($r = 0.5$, $p = 0.14$), but a significant large negative association on the regional level ($r = -0.87$, $p = 1 \times 10^{-74}$). The lack of significance of the former effect is potentially due to the small sample size of 10 participants. In the six state transitions we studied, we found a significant large positive correlation between minimum and optimal control energy both on the individual level ($r = 0.99$, $p = 1 \times 10^{-7}$) and on the regional level ($r = 0.97$, $p = 1 \times 10^{-136}$). Consistent with the mathematical constraints of their definitions, minimum control energy was significantly lower than optimal control energy on both the individual ($mean_{min} = 43.8$, $mean_{opt} = 56.0$, $V = 0$, $p = 2 \times 10^{-3}$) and regional ($mean_{min} = 0.19$, $mean_{opt} = 0.24$, $V = 2$, $p = 6 \times 10^{-40}$) levels. Finally, we investigated how controllability metrics and control energies are related. On both levels of examination, average controllability demonstrated small negative correlations with control energies (ranging from $r = -0.29$, $p = 6 \times 10^{-6}$ to $r = -0.03$, $p = 0.93$), whereas modal controllability showed slightly larger, positive associations with control energies (ranging from $r = 0.23$, $p = 3 \times 10^{-4}$ to $r = 0.45$, $p = 0.19$). The size of the correlations estimated with empirical data supported the scarcity of a clear theoretical link between the concepts. Yet, the directions of the effects was consistent with the general notion that high average controllability implies low control energy, whereas modal controllability is linked to higher control energies.

3.3 Complexity of energy landscape in discrete-time systems

In the main text, we report a high consistency of the complexity of the energy landscape across time-systems ($r = 0.87$, $p = 1 \times 10^{-3}$). Thus and for brevity, in the main text we report results for continuous-time systems only. Here for completeness we wished to additionally validate the newly developed metric in discrete-time systems. Similar to continuous-time systems, we observed a small negative association of the complexity of the energy landscape with average controllability ($r = -0.09$, $p = 0.80$), a large negative association with modal controllability ($r = -0.74$, $p = 0.01$), and a small negative association with minimum control energy ($r = -0.12$, $p = 0.74$). The significantly lower complexity of the energy landscape of brain networks compared to topological ($W = 430$, $p = 6 \times 10^{-7}$), spatial ($W = 1$, $p = 5 \times 10^{-8}$), and combined null models ($W = 3062$, $p = 0.03$) in discrete-time systems (SFig. 9) was also in line with findings in continuous-time systems. Again, the combination of topological and spatial characteristics seemed to partially explain the higher homogeneity of the energy landscape of the brain. Finally, we also found a negative, yet not significant Pearson correlation with age ($r = -0.56, p = 0.09$) in discrete-time systems. Taken together, the metric yielded highly consistent results across discrete- and continuous-time systems.

4 Supplementary Discussion

4.1 Expanding horizons of network control theory.

New developments in network control theory are constantly expanding the horizons of research questions that can be tackled with the associated tools. Many (but perhaps not all) of these developments could be helpful in the study of the mind and brain. Efforts have recently revealed a relation between controllability and symmetry [13–15], which could prove useful in determining the impact of bilateral and other symmetries on neural dynamics. The field has begun considering multiobjective functions, tradeoffs, and constraints in control [16, 17], in addition to probing a system's potential for control via local topological information [18]. As the field of neuroscience moves more concertedly towards multimodal approaches, efforts in the control of multilayer networks could prove particularly useful [19], as could methods for detecting control nodes across scales [20–22]. For some questions, advances in the control of nonlinear systems could prove effective [23–25], including applications of Ising models [26, 27] and considerations related to the dynamics of neural mass models [28]. Finally, moving beyond network controllability, recent work expanding system identification methods to identify specific form of nonlinear dynamics present in brain is particularly promising [29–31].
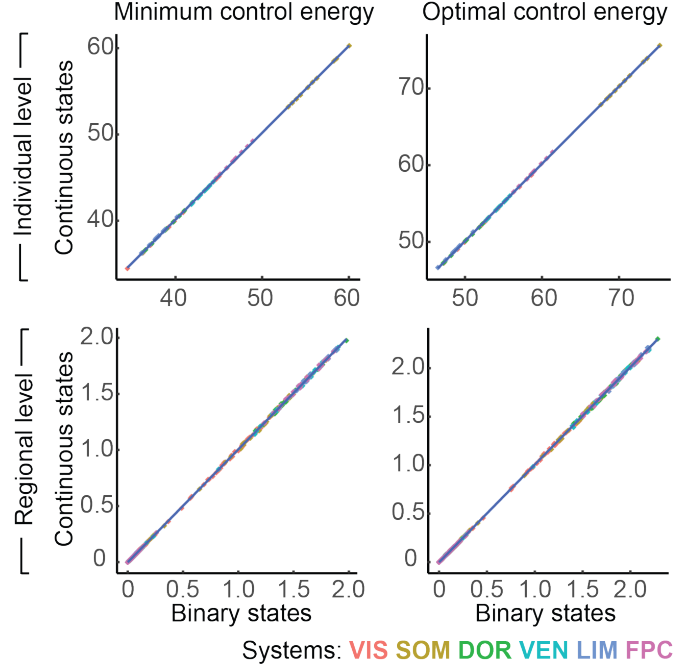
5 Supplementary Figures

Figure 1: **Consistent control energies across binary and continuous state representations.** *(A)* Minimum and *(B)* optimal control energy for state transitions from activation of the default mode system to activation of six target cognitive systems. Continuous initial and target states were generated by randomly adding uniformly distributed noise in the range of 0.001 to 0.01 to the binary states. Based on a whole brain control set including all 233 brain regions. Colored dots represent *(Top)* individuals and *(Bottom)* brain regions. Blue line represents Pearson correlation between binary and continuous state representations. We observed a high consistency of control energy between binary and continuously represented brain states on both the individual ($r_{min} = 0.99$, $p_{min} = 2 \times 10^{-16}$; $r_{opt} = 0.99$, $p_{opt} = 2 \times 10^{-16}$) and regional level ($r_{min} = 0.99$, $p_{min} = 2 \times 10^{-16}$; $r_{opt} = 0.99$, $p_{opt} = 2 \times 10^{-16}$). Abbreviations: VIS = visual, SOM = somatomotor, DOR = dorsal attention, VEN = ventral attention, LIM = limbic, and FPC = frontoparietal control.
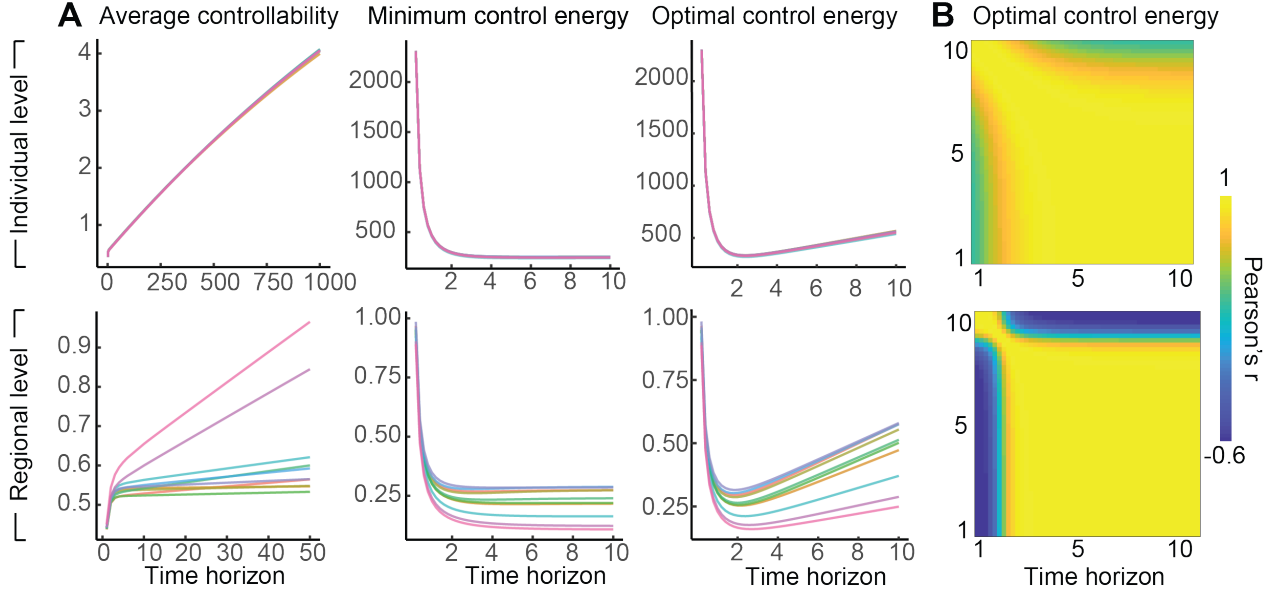
Figure 2: **Impact of time horizon on average controllability metrics and control energies.** *(A)* Average controllability, minimum control energy, and optimal control energy depending on different choices of time horizon T. *(Top)* Colored lines represent individual values summarized across brain regions. *(Bottom)* Colored lines represent exemplary regional metrics from 10 randomly selected brain regions. *(B)* Consistency of average controllability and minimum control energy across time horizons. Heat maps depict correlation matrices of different time horizons. Each heat map entry corresponds to the Pearson correlation of a metric estimated at one choice of the time horizon and the same metric estimated at a second choice of the time horizon. *(Top)* Pearson correlation of individual metrics summarized across brain regions. *(Bottom)* Pearson correlation of regional metrics averaged across participants.
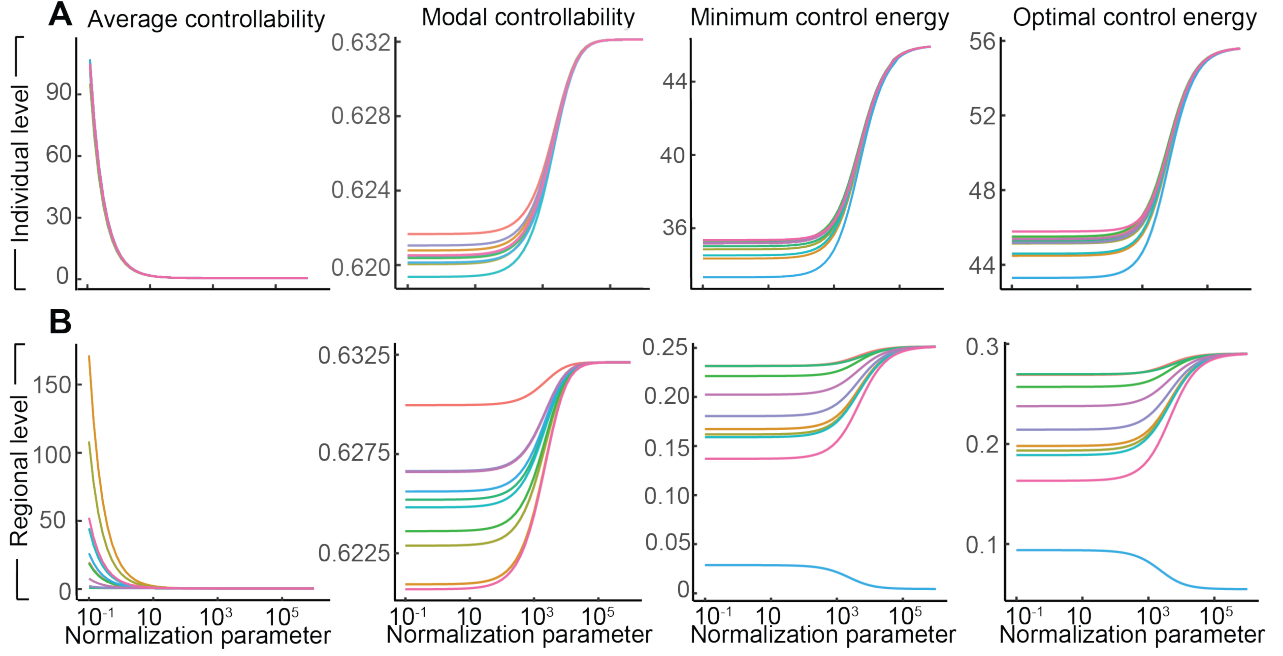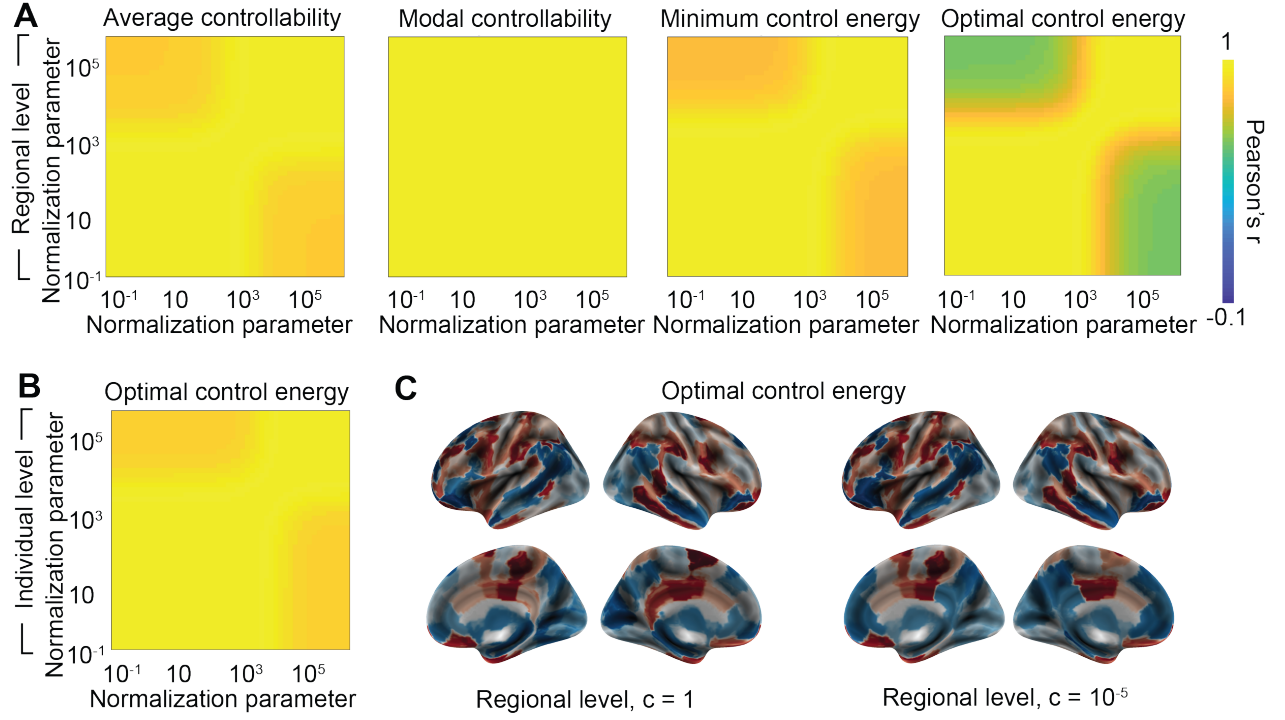
Figure 3: **Impact of normalization on controllability metrics and control energies.** Average controllability, modal controllability, minimum control energy, and optimal control energy depending on different choices of normalization parameter c. *(Top)* Colored lines represent individual values summarized across brain regions. *(Bottom)* Colored lines represent exemplary regional metrics from 10 randomly selected brain regions. Normalizing the system such that it stabilizes faster decreased average controllability and increased modal controllability and control energies on both the individual and regional level.

Figure 4: **Different control regimes depending on normalization.** Consistency of controllability metrics and control energies for different choices of the normalization parameter c. *(A)* Heat maps depict correlation matrices of average controllability, modal controllability, minimum control energy, and optimal control energy based on different normalization parameters. Pearson correlation of regional metrics summarized across individuals. *(B)* Heat maps depict correlation matrices of optimal control energy based on different normalization parameters. Pearson correlation of individual optimal control energy summarized across brain regions. Normalizing the system such that it stabilizes faster introduced a different control regime. *(C)* Regional optimal control energy projected onto the brain surface using normalization parameters of $c = 1$ and $c = 10^5$ to illustrate the alternative control regimes. Note that the metric values are ranked for visualization purposes only.
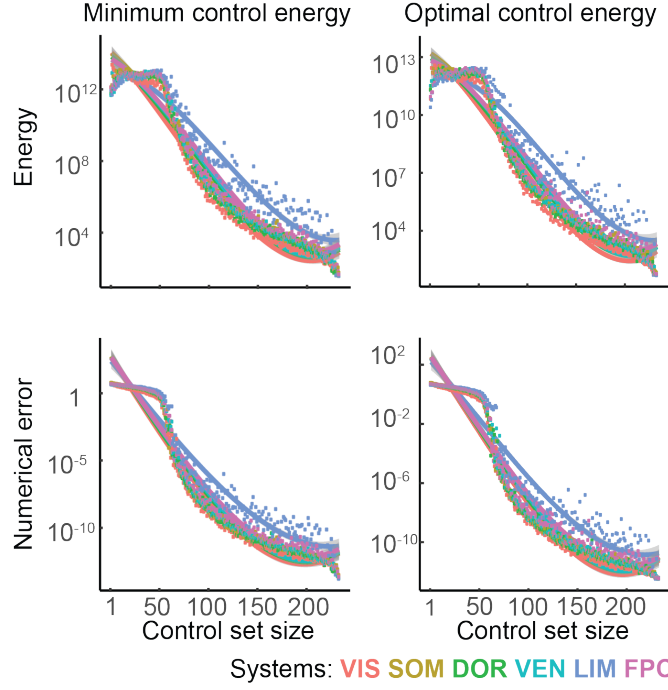
Figure 5: **Impact of control node set size on control energies.** Minimum and optimal control energy for state transitions from activation of the default mode system to activation of six target cognitive systems (colored dots and lines) based on a varying number of controlled brain regions. *(Top)* Control energies and *(Bottom)* associated numerical error during the calculation monotonically decreased with increasing control set sizes. All values are averaged across participants. Lines and ribbons represent the best fit to the data and the 95% confidence interval, respectively. Abbreviations: VIS = visual, SOM = somatomotor, DOR = dorsal attention, VEN = ventral attention, LIM = limbic, and FPC = frontoparietal control.
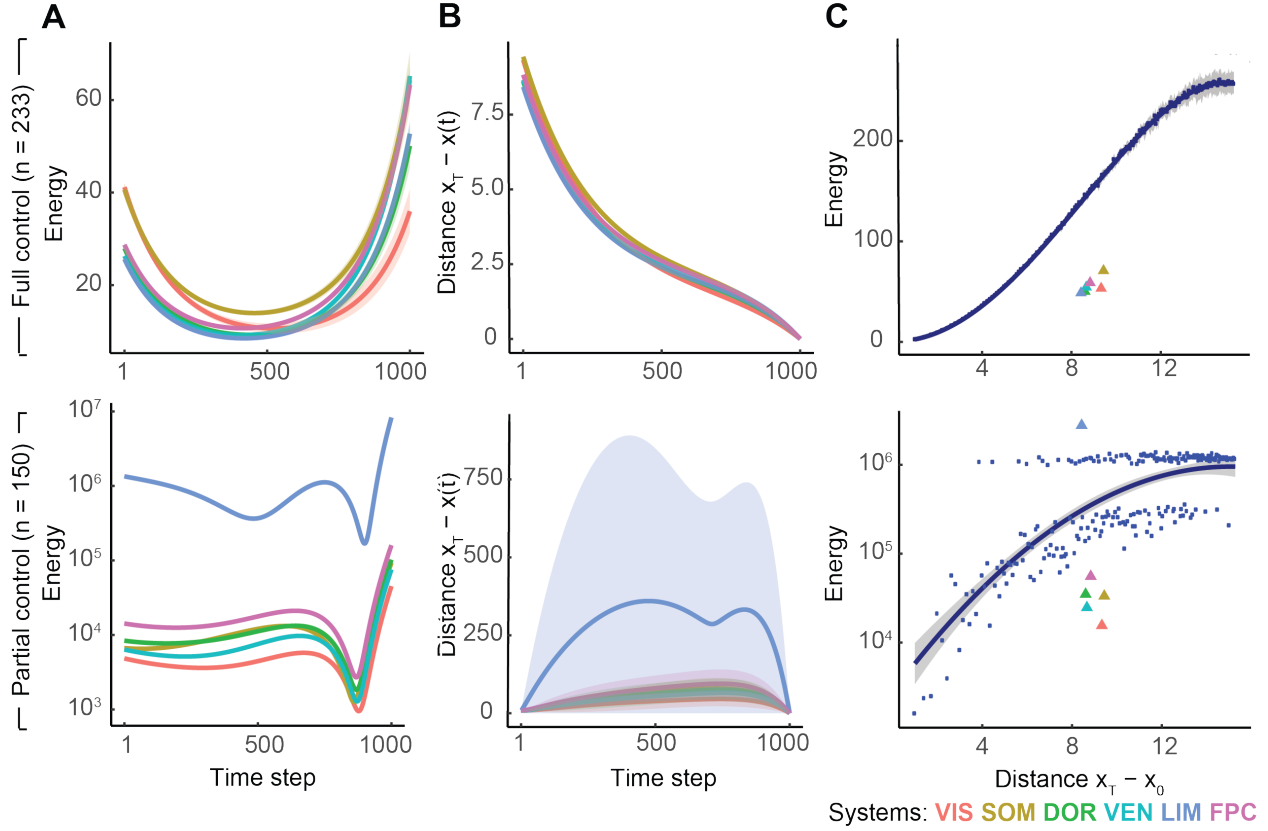
13

Figure 6: **Optimal control energy in full and partial control sets.** Optimal control energy for state transitions from activation of the default mode system to activation of six target cognitive systems (colored lines and triangles). *(Top)* Based on a whole brain control set including all 233 brain regions. *(Bottom)* Control set consists of random subsets of 150 brain regions. *(A)* The optimal control energy across control trajectory differed between different control set sizes. *(B)* The Euclidean distance between the current state and the target state across the control trajectory differed between control set sizes.*(C)* The optimal control energy increases with larger Euclidean distance between the initial state and the target state. Blue dots depict state transitions from a zero-activity brain state to a varying number of randomly activated brain regions. All values are averaged across participants. Lines and ribbons represent the best fit to data and the 95% confidence interval, respectively. Abbreviations: x_0 = initial state, x_T = target state, $x(t)$ = state at time t, VIS = visual, SOM = somatomotor, DOR = dorsal attention, VEN = ventral attention, LIM = limbic, and FPC = frontoparietal control.
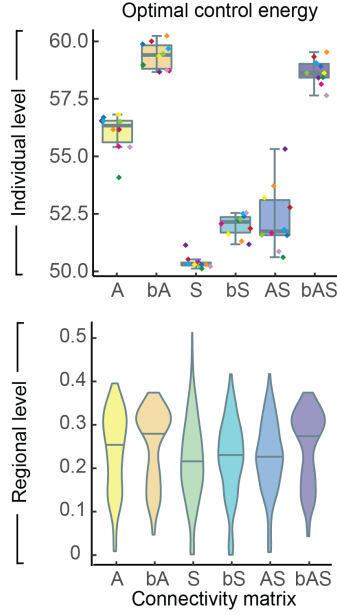
14

Figure 7: **Structural connectivity measures.** Optimal control energy for different measures of structural connectivity. The network encoded by the adjacency matrix $\boldsymbol{A}$ is based on streamline counts from diffusion imaging. The network encoded by the adjacency matrix $\boldsymbol{S}$ is based on spatial adjacency between two brain regions from T1-weighted images. The network encoded by the adjacency matrix $\boldsymbol{AS}$ is an average of $\boldsymbol{A}$ and $\boldsymbol{S}$. Here we also considered the influence of converting the weighted networks into binary versions ($\boldsymbol{bA}, \boldsymbol{bS}, \boldsymbol{bAS}$). *(Top)* Box plots depict individual controllability metrics and control energy summarized across brain regions. Colored diamonds represent individuals and provide insight into individual changes. *(Bottom)* Violin plots show regional metrics averaged across participants. The two structural connectivity measures provide complementary information that is retained by their combination.
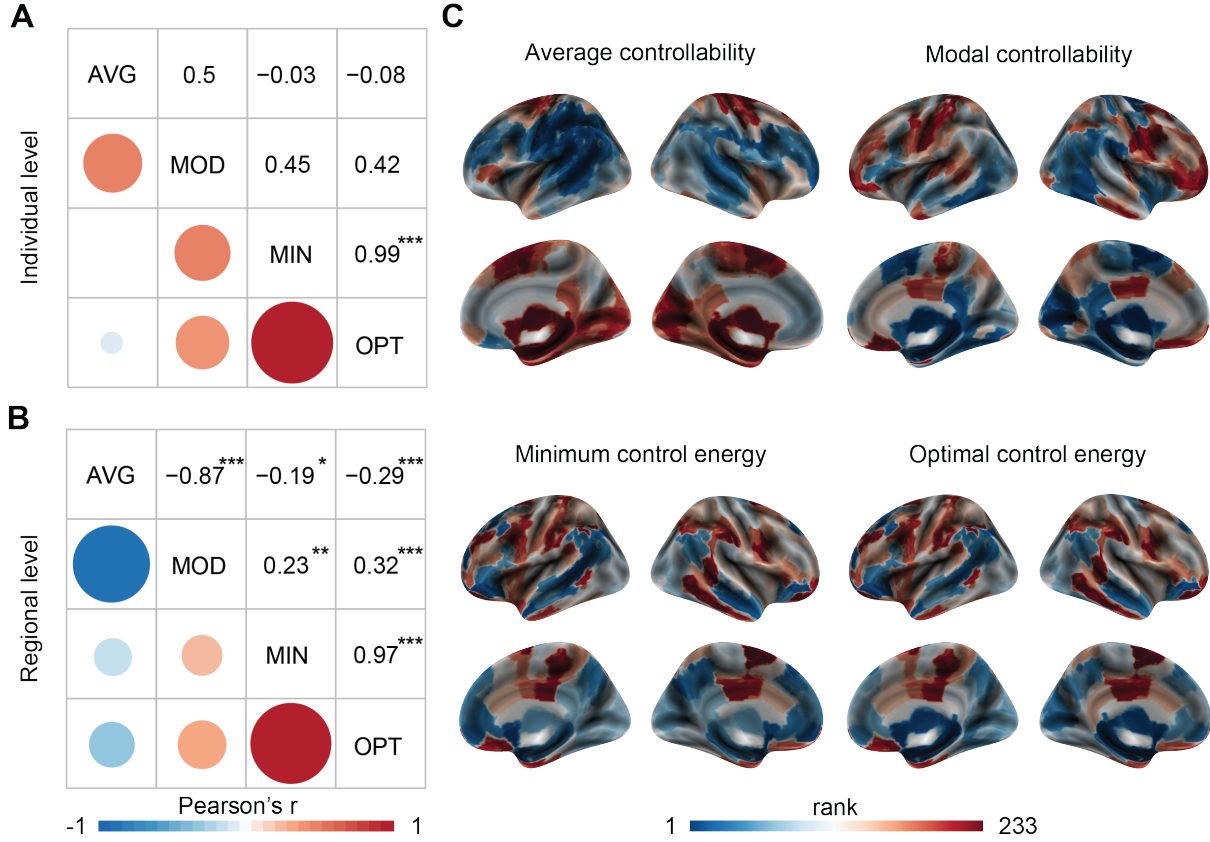
Figure 8: **Relation between controllability metrics and control energies.** *(A)* The correlation matrix of individual average controllability, modal controllability, minimum control energy, and optimal control energy, summarized across brain regions. Pearson correlation coefficients (upper matrix triangle) additionally encoded via color and size of circles (lower matrix triangle). *(B)* Analogously, the correlation matrix of regional controllability metrics and control energies averaged across participants. *(C)* Regional controllability metrics and control energies projected onto the brain surface. Note that the metric values are ranked for visualization purposes only. Collectively, these panels illustrate the negative association between regional average and modal controllability, and the high consistency between minimum and optimal control energy. Abbreviations: AVG = average controllability, MOD = modal controllability, MIN = minimum control energy, and OPT = optimal control energy. Asterisks indicate significance on a Bonferroni-corrected α-level of 0.05 (*), 0.01 (**), and 0.001 (***).
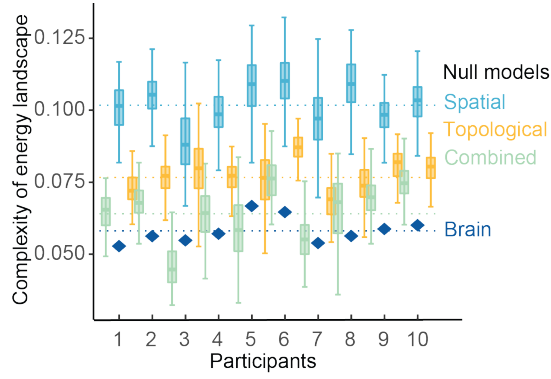
16

Figure 9: **Complexity of the energy landscape of the human brain in discrete time.** Heterogeneity of the minimum control energy landscape of individual participants (dark blue diamonds) to three null models preserving different characteristics of the brain networks. The complexity of the energy landscape was quantified by the variability of the eigenvalue distribution of the discrete-time controllability Gramian. Null model distributions (box plots) were estimated by randomly rewiring each brain network 100 times. Spatial null models (blue box plots) preserved the relationship between edge weight and Euclidean distance. Topological null models (yellow box plots) preserved the degree and strength distributions. Combined null models (green box plots) preserved both the strength distribution and the relationship between edge weight and Euclidean distance. Dashed lines indicate the complexity of the energy landscape of brain networks and null models averaged across individuals. The combination of topological and spatial characteristics partially explains the homogeneous energy landscape of the brain.
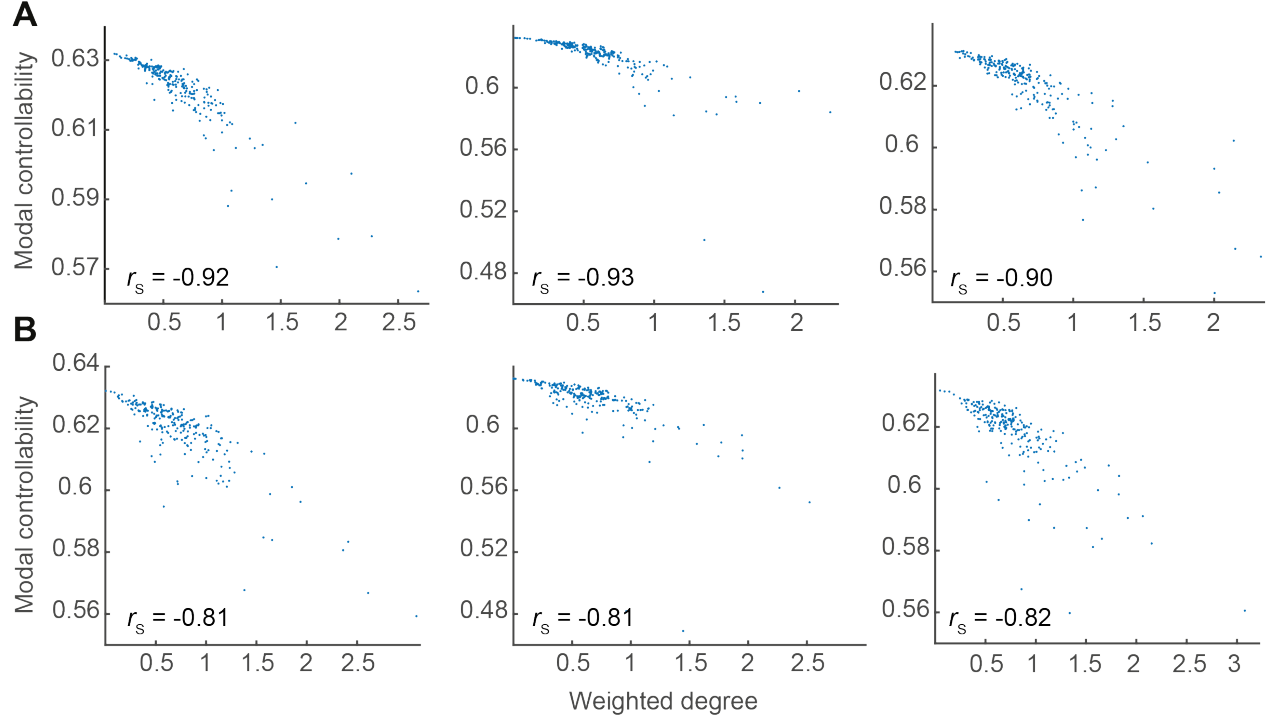
Figure 10: **Relationship between modal controllability and weighted degree.** *(A)* Association between modal controllability and weighted degree of a node in three exemplary brain networks. Across the 10 brain networks, Spearman's rank correlation coefficients (r_S) ranged from $r_S = -0.94$ to $r_S = -0.90$ $(p-values < 0.001)$. *(B)* Association between modal controllability and weighted degree of a node in corresponding random network null models that preserved the weighted degree distribution of the brain networks [32]. Across 100 instantiations of the null models, the Spearman's rank correlation coefficients ranged from $r_S = -0.85$ to $r_S = -0.80$ $(p-values < 0.001)$ on average. The association of modal controllability and weighted degree was significantly larger in brain networks compared to the null models $(p < 0.001)$.
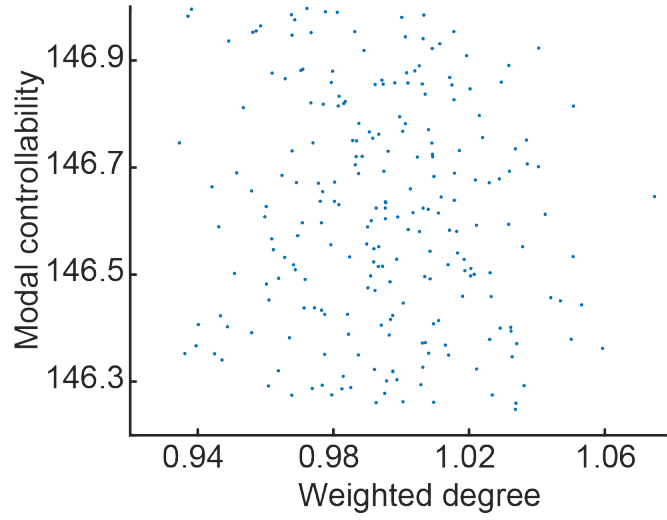
Figure 11: **An example network that exhibits no correlation between modal controllability and weighted degree.** Association between modal controllability and weighted degree of a node in a symmetric negative definite matrix. The network was generated by randomly sampling from uniformly distributed values between 0 and 1 to weight each edge in the network. Then, we normalized the continuous-time system. In this example, the Spearman's rank correlation coefficient (r_S) between modal controllability and weighted degree of a node was not significant ($r_S = -0.08, p = 0.20$), demonstrating that the two metrics are unrelated mathematically.

References

[1] F. Pasqualetti, S. Zampieri, F. Bullo, Controllability metrics, limitations and algorithms for complex networks, IEEE Transactions on Control of Network Systems 1 (1) (2014) 40–52.

[2] S. Gu, F. Pasqualetti, M. Cieslak, Q. K. Telesford, B. Y. Alfred, A. E. Kahn, J. D. Medaglia, J. M. Vettel, M. B. Miller, S. T. Grafton, et al., Controllability of structural brain networks, Nature communications 6 (2015) 8414.

[3] B. Marx, D. Koenig, D. Georges, Optimal sensor and actuator location for descriptor systems using generalized gramians and balanced realizations, in: Proceedings of the 2004 American Control Conference, Vol. 3, IEEE, 2004, pp. 2729–2734.

[4] H. R. Shaker, M. Tahavori, Optimal sensor and actuator location for unstable systems, Journal of Vibration and Control 19 (12) (2013) 1915–1920.

[5] E. Nozari, F. Pasqualetti, J. Cortés, Heterogeneity of central nodes explains the benefits of time-varying control scheduling in complex dynamical networks, Journal of Complex Networks (2019).

[6] J. Z. Kim, J. M. Soffer, A. E. Kahn, J. M. Vettel, F. Pasqualetti, D. S. Bassett, Role of graph architecture in controlling dynamical networks with applications to neural systems, Nature physics 14 (1) (2018) 91.

[7] K. Gorgolewski, C. D. Burns, C. Madison, D. Clark, Y. O. Halchenko, M. L. Waskom, S. S. Ghosh, Nipype: a flexible, lightweight and extensible neuroimaging data processing framework in python., Front Neuroinform 5 (08 2011).

[8] B. B. Avants, N. J. Tustison, G. Song, P. A. Cook, A. Klein, J. C. Gee, A reproducible evaluation of ants similarity metric performance in brain image registration, Neuroimage 54 (3) (2011) 2033–2044.

[9] F.-C. Yeh, V. J. Wedeen, W.-Y. I. Tseng, Generalized q-sampling imaging, IEEE transactions on medical imaging 29 (9) (2010) 1626–1635.

[10] F.-C. Yeh, T. D. Verstynen, Y. Wang, J. C. Fernández-Miranda, W.-Y. I. Tseng, Deterministic diffusion fiber tracking improved by quantitative anisotropy, PloS one 8 (11) (2013) e80713.

[11] M. Cieslak, S. Grafton, Local termination pattern analysis: a tool for comparing white matter morphology, Brain imaging and behavior 8 (2) (2014) 292–299.

[12] D. S. Bassett, J. A. Brown, V. Deshpande, J. M. Carlson, S. T. Grafton, Conserved and variable architecture of human white matter connectivity, Neuroimage 54 (2) (2011) 1262–1279.

[13] A. J. Whalen, S. N. Brennan, T. D. Sauer, S. J. Schiff, Observability and controllability of nonlinear networks: The role of symmetry, Phys Rev X 5 (2015) 1.

[14] C. Zhao, W. X. Wang, Y. Y. Liu, J. J. Slotine, Intrinsic dynamics induce global symmetry in network controllability, Sci Rep 5 (8422) (2015).

[15] A. J. Whalen, S. N. Brennan, T. D. Sauer, S. J. Schiff, Effects of symmetry on the structural controllability of neural networks: A perspective, Proc Am Control Conf 2016 (2016) 5785–5790.

[16] Y. Tang, H. Gao, W. Du, J. Lu, A. V. Vasilakos, J. Kurths, Robust multiobjective controllability of complex neuronal networks, IEEE/ACM Trans Comput Biol Bioinform 13 (4) (2016) 778–791.

[17] H. Keren, S. Marom, Controlling neural network responsiveness: tradeoffs and constraints, Front Neuroeng 7 (2014) 11.

[18] G. Li, L. Deng, G. Xiao, P. Tang, C. Wen, W. Hu, J. Pei, L. Shi, H. E. Stanley, Enabling controlling complex networks with local topological information, Sci Rep 8 (1) (2018) 4593.

[19] G. Menichetti, L. Dall'Asta, G. Bianconi, Control of multilayer networks, Sci Rep 6 (2016) 20706.

[20] Y. Tang, H. Gao, J. Kurths, Multiobjective identification of controlling areas in neuronal networks, IEEE/ACM Trans Comput Biol Bioinform 10 (3) (2013) 708–720.

[21] Y. Tang, Z. Wang, H. Gao, S. Swift, J. Kurths, A constrained evolutionary computation method for detecting controlling regions of cortical networks, IEEE/ACM Trans Comput Biol Bioinform 9 (6) (2012) 1569–1581.

[22] Y. Tang, H. Gao, W. Zou, J. Kurths, Identifying controlling nodes in neuronal networks in different scales, PLoS One 7 (7) (2012) e41375.

[23] S. P. Cornelius, W. L. Kath, A. E. Motter, Realistic control of network dynamics, Nat Commun 4 (2013) 1942.

[24] A. E. Motter, Networkcontrology, Chaos 25 (9) (2015) 097621.

[25] J. G. T. Zañudo, G. Yang, R. Albert, Structure-based control of complex networks with nonlinear dynamics, Proceedings of the National Academy of Sciences 114 (28) (2017) 7234–7239.

[26] C. W. Lynn, D. D. Lee, Statistical mechanics of influence maximization with thermal noise, European Physics Letters 117 (2017).

[27] S. Gu, M. Cieslak, B. Baird, S. F. Muldoon, S. T. Grafton, F. Pasqualetti, D. S. Bassett, The energy landscape of neurophysiological activity implicit in brain network structure, Sci Rep 8 (1) (2018) 2507.

[28] X. Liu, J. Gao, G. Wang, Z. W. Chen, Controllability analysis of the neural mass model with dynamic parameters, Neural Comput 29 (2) (2017) 485–501.

[29] C. O. Becker, D. S. Bassett, V. M. Preciado, Large-scale dynamic modeling of task-fMRI signals via subspace system identification, J Neural Eng 15 (6) (2018) 066016.

[30] A. Ashourvan, S. Pequito, M. Bertolero, J. Z. Kim, D. S. Bassett, B. Litt, A dynamical systems framework to uncover the drivers of large-scale cortical activity, bioRxiv 638718 (2019).

[31] G. Koppe, J. Toutounji, P. Kirsch, S. Lis, D. Durstewitz, Identifying nonlinear dynamical systems via generative recurrent neural networks with applications to fMRI, arXiv 1902 (2019) 07186.

[32] M. Rubinov, O. Sporns, Complex network measures of brain connectivity: uses and interpretations, Neuroimage 52 (3) (2010) 1059–1069.